Bio-Design and Manufacturing (2020) 3:410–426
https://doi.org/10.1007/s42242-020-00083-7

RESEARCH ARTICLE

Precise robust motion control of cell puncture mechanism driven by piezoelectric actuators with fractional-order nonsingular terminal sliding mode control

Shengdong Yu[1,2] · Hongtao Wu[2] · Mingyang Xie[2] · Haiping Lin[3] · Jinyu Ma[1,2]

Received: 30 March 2020 / Accepted: 9 June 2020 / Published online: 26 July 2020

Abstract

A novel robust controller is proposed in this study to realize the precise motion control of a cell puncture mechanism (CPM) driven by piezoelectric ceramics (PEAs). The entire dynamic model of CPM is constructed based on the Bouc–Wen model, and the nonlinear part of the dynamic model is optimized locally to facilitate the construction of a robust controller. A model-based, nonlinear robust controller is constructed using time-delay estimation (TDE) and fractional-order nonsingular terminal sliding mode (FONTSM). The proposed controller does not require prior knowledge of unknown disturbances due to its real-time online estimation and compensation of unknown terms by using the TDE technology. The controller also has finite-time convergence and high-precision trajectory tracking capabilities due to FONTSM manifold and fast terminal sliding mode-type reaching law. The stability of the closed-loop system is proved by Lyapunov stability theory. Computer simulation and hardware-in-loop simulation experiments of CPM verify that the proposed controller outperforms traditional terminal sliding mode controllers, such as the integer-order or model-free controller. The proposed controller can also continuously output without chattering and has high control accuracy. Zebrafish embryo is used as a verification target to complete the cell puncture experiment. From the engineering application perspective, the proposed control strategy can be effectively applied in a PEA-driven CPM.

Keywords Cell puncture mechanism (CPM) · Piezoelectric actuator (PEA) · Robust motion control · Fractional-order nonsingular terminal sliding mode (FONTSM) · Time-delay estimation (TDE)

Introduction

Microinjection is a micromanipulation technology that can complete biological operations in cells or embryos [1]. Specifically, microinjection can be used to inject micrometric external substances, such as drugs, sperm, DNA, protein, and RNA, into living cells [2]. Biologists can complete a series of medical research, such as in gene engineering, virus detection [3], drug development, and disease analysis [4], by observing the growth and development of cells [5]. Accordingly, microinjection has attracted the attention of many scholars [6], which has resulted in the development of many cell manipulation methods [7], such as cell localization, puncture, and injection [8]. Among these methods, cell puncture is a prerequisite of cell microinjection that uses an injecting pipette to penetrate the cell membrane and accurately locate in the designated cell tissue [9]. However, cells are small [10], easy to deform, and fragile in vitality [11]. The specific physiological characteristics of cells also require high tech-

✉ Jinyu Ma
jinyuma@nuaa.edu.cn

Shengdong Yu
shengdong@nuaa.edu.cn

Hongtao Wu
methwu@126.com

Mingyang Xie
myxie@nuaa.edu.cn

Haiping Lin
709685904@qq.com

1 Wenzhou Polytechnic, Wenzhou 325000, China

2 Nanjing University of Aeronautics and Astronautics, Nanjing 210016, China

3 Hangzhou Vocational and Technical College, Hangzhou 310000, China

nical requirements for cell puncture [12]. Therefore, a robust controller must be developed for a cell puncture mechanism (CPM) to achieve a sufficient precise motion control.

CPM is a mechanical and electrical integration equipment that can realize submicron-level high-precision micro/nano-operations in a sterile environment. As a newly developed intelligent driving material, piezoelectric ceramics (PEAs) [13] have no gap, no electromagnetic pollution, no noise pollution, high resolution, and large driving force [14]. Compared with other traditional hydraulic or motor drive systems, PEAs have unparalleled advantages in the field of micro-operation. However, PEAs also have obvious defects, including their limited motion range (usually within 30 microns), substantial hysteresis, creep, high-frequency vibration, and other nonlinear effects [15]. A displacement amplification mechanism must then be designed to amplify the output displacement of PEAs [16]. However, the displacement amplification mechanism can also amplify the hysteretic nonlinear effect. Therefore, the development of a high-precision, robust controller suitable for CPM presents a challenge.

A charge-driven control method based on constant current and high impedance can eliminate the hysteretic nonlinear effect of PEAs [17]. However, the charge driving circuit is highly complex and reduces the effective stroke of PEAs [18]. Many scholars have studied dynamic models of PEAs with hysteretic nonlinear effects [19–23]. These models provide strong theoretical support for the design of robust controllers yet often use nonlinear equations with complex structures and numerous parameters to depict the hysteretic nonlinear effect. Identifying the parameters of nonlinear equations is also a tedious and time-consuming process [24]. Therefore, hysteretic nonlinearity and external disturbance are considered unknown terms that can simplify the dynamic model to facilitate the engineering application and design of robust controllers. In robust control, sliding mode control (SMC) [25] can effectively handle the model defects and uncertainties in a nonlinear system [26], thereby making this technology suitable for the motion control of CPM.

In SMC, the displacement error and its derivatives are taken as the current state of the system [27]. The structure of the system continuously changes along with the current state and moves according to the predetermined "sliding mode" state trajectory [28]. Traditional SMC uses the linear sliding surface [29], which ensures that the state trajectory achieves progressive convergence [30]. Finite-time stability can significantly improve the performance of the controller and achieve finite-time convergence [31]. A nonsingular TSM (NTSM) [32] has been proposed to overcome the singular problem, and a fast-TSM-type reaching law has been developed to suppress chattering. Fast NTSM (FNTSM), which is achieved by synthesizing NTSM manifold and fast-TSM-type reaching law, has continuous output, no chattering, and precise control [33]. However, the existing FNTSM is mostly limited to using an integer-order (IO) differentiator or integrator. The fractional-order (FO) controller has been recently proven to outperform the IO controller [34]. Therefore, the performance of the FNTSM controller can be improved by synthesizing FO theory and FNTSM controller. Prior knowledge of the unknown quantity boundary of the system, whether by using FNTSM or FO NTSM (FONTSM), is also required due to the unknown terms in the dynamic model of CPM. Moreover, the selection of the gain coefficient of the robust term in the controller tends to be conservative, which damages the quality of the controller. Therefore, an accurate estimation of unknown terms must be ensured.

Time-delay estimation (TDE) [35] estimates the current system state in real time from the previous system state in a closed-loop control to realize online estimation and real-time compensation for unknown items in time-delay control (TDC) [36]. TDE technology has been widely studied and applied because of its reduced dependence on the model and easy engineering application. Therefore, the nonlinear, robust controller designed by synthesizing FONTSM and TDE has strong advantages. TDE realizes a real-time estimation and compensation of unknown terms and reduces the gain coefficient in FONTSM, whereas FONTSM realizes an effective time convergence and improves control accuracy.

However, TDE has several disadvantages in practical applications that are mainly reflected in two aspects. First, in this technology, the value of time-delay parameter L must be minimized to improve the accuracy of estimating unknown items, but the adjustment of L is restricted by the electrical hardware system. Second, in TDE, both velocity and acceleration information must be known, but only a displacement sensor is often set up in practical applications. The velocity signal can be obtained by one differential calculation for the displacement signal, whereas the acceleration signal can be obtained by performing two differential calculations for the displacement signal. However, the measurement noise is greatly amplified in the differential calculation, thereby resulting in large errors in both velocity and acceleration signals. Despite realizing model-free control, TDC has substantial unknown items. In this case, controller quality can only depend on the realization of TDE technology. In the model-based controller, the proportion of unknown items in the system is effectively restrained, thereby suppressing the estimation error of TDE. Another advantage of this method is that the controller quality depends on the common implementation of FONTSM and TDE.

The major contributions of this paper are summarized as follows. First, FONTSM and TDE are synthesized to construct a nonlinear robust controller called FONTSM-TDE. Second, the hysteresis dynamic model of CPM is constructed and optimized locally. A model-based FONTSM-TDE is proposed for the first time in this paper. The stability of FONTSM-TDE is demonstrated by using Lyapunov theory.

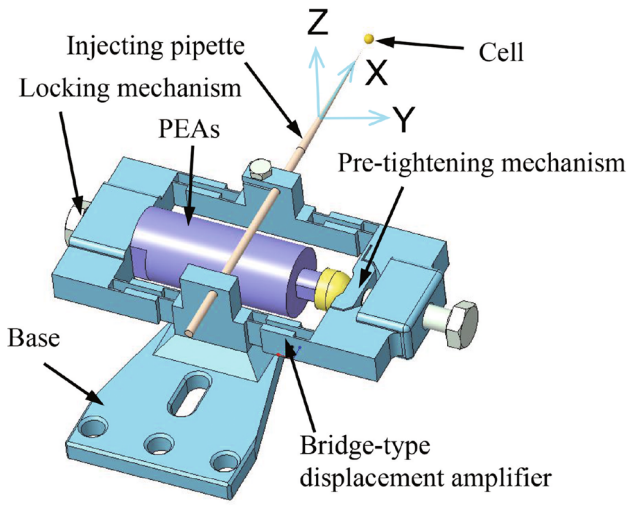

Fig. 1 Three-dimensional virtual prototype of CPM

Third, a cell puncture experiment is performed on zebrafish embryo to validate the effectiveness of the designed CPM and the proposed controller.

The rest of this paper is arranged as follows. Section 2 designs and manufactures CPM and constructs the dynamic model. Section 3 completes the controller design and stability analysis. Sections 4 and 5 present a computer simulation and hardware-in-loop simulation (HILS) experiment, respectively. Section 6 conducts a cell puncture experiment on zebrafish embryos and, finally, summarizes the paper.

CPM

Mechanical structure design of CPM

A bridge-type displacement amplification mechanism (BTD /AM) is designed based on the compliant mechanism principle, which does not bring driving clearance to CPM, thereby ensuring a high-precision motion effect. Figure 1 shows the 3D virtual prototype of CPM. The two ends of PEAs are separately fixed to the BTDAM by a locking and preloading mechanism. This scheme eliminates the connection gap and applies a certain preload to the PEAs. The centroid of the injecting pipette is locked to the BTDAM, whereas the tail is slidably connected to the guiding hole to ensure that the injecting pipette strictly moves along a straight line.

When PEAs are extended, the flexure hinge of BTDAM is elastically deformed. This condition drives the injection pipette to output a large displacement. The flexure hinge can be multi-objectively optimized by using a finite element simulation and optimization technology. The flexure hinge can obtain the maximum displacement magnification and the highest natural frequency to ensure strength. Refer to [27] for the optimal design of BTDAM. Although the mechanical structure of BTDAM is highly complex, 3D printing technology is suitable for rapid prototyping.

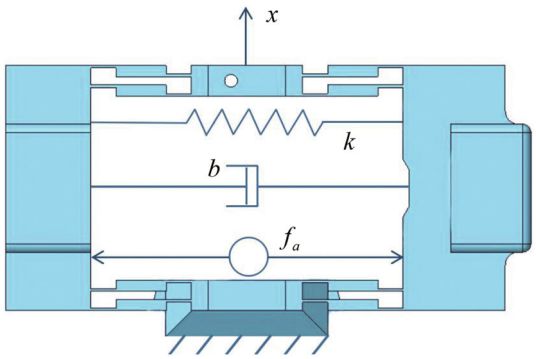

Fig. 2 Equivalent dynamic model of CPM

Dynamic model of CPM

The equivalent dynamic model of CPM is established as a mass-spring-damping system as shown in Fig. 2. Parameters b, k, and f_a denote the output forces of PEAs, damping coefficient, and stiffness coefficient of the system, respectively.

A complete dynamic model of CPM with hysteresis is constructed to comprehensively reflect the dynamic characteristics of the system by using Newton's law of motion and the Bouc–Wen model [37]. The dynamic model can be expressed as

$$m\ddot{x} + b\dot{x} + kx = f_a - \tau_d = k(du - h) - \tau_d, \tag{1}$$

$$\dot{h} = \zeta_1 d\dot{u} - \zeta_2|\dot{u}|h - \zeta_3\dot{u}|h|, \tag{2}$$

where m, d, h, and τ_d are the mass, piezoelectric coefficient, hysteresis variable, and external disturbance, respectively; x, $\dot{x}$, and $\ddot{x}$ are the actual displacement, velocity, and acceleration, respectively; and ζ_1, ζ_2, and ζ_3 are the hysteresis coefficients.

The dynamic model is then simplified reasonably, and the complexity of the model is reduced to ensure its integrity as much as possible and to facilitate the engineering application and design of the robust controller. Equation (1) can be rewritten as

$$\ddot{x} = \frac{kdu}{m} - \frac{kh}{m} - \frac{b}{m}\dot{x} - \frac{kx}{m} + \frac{\tau_d}{m}. \tag{3}$$

The hysteresis term and external disturbance are combined as follows into an unknown term:

$$\Delta P(m, k, h, \tau_d) = -\frac{k}{m}h + \frac{\tau_d}{m}. \tag{4}$$

In Eqs. (2) and (4), the unknown term can be regarded as nonlinear terms that include hysteresis, external disturbance, and unmodeled dynamics. This unknown term has a highly complex composition, and an accurate mathematical model cannot be established. For convenience, $\Delta P(m, k, h, \tau_d)$ is abbreviated as ΔP.

Equation (5) is rewritten as follows to obtain a new dynamic model:

$$\ddot{x} = \frac{kd}{m}u - \frac{b}{m}\dot{x} - \frac{k}{m}x + \Delta P. \tag{5}$$

Remark 1 All nonlinear terms are summed as unknown terms, and only a linear term exists in the optimized dynamic model [Eq. (5)]. Accordingly, the parameter identification efficiency is greatly improved, and nonlinear parameter identification is transformed into linear parameter identification that is conducive to engineering applications.

Hysteretic effect

The voltage displacement curve (Fig. 3b) can be obtained by applying a sine wave voltage (Fig. 3a) whose amplitude and frequency decrease continuously with time. A strong nonlinear phenomenon is observed between the voltage and displacement, and the relationship between these two demonstrates a multivalued mapping. The voltage displacement curve shows an elliptical hysteresis loop, and different voltage amplitudes correspond to different hysteresis loops.

Parameter identification of dynamic model

Parameter m in the dynamic model [Eq. (5)] is measured as $m = 0.0225$ kg by using an electronic balance, and the other parameters must be obtained via parameter identification. A low-frequency, low-amplitude excitation voltage can effectively suppress the hysteretic effect of PEAs, and a low-amplitude, low-frequency sine wave sweep voltage is applied to PEAs (e.g., the voltage amplitude is 3 V, and the frequency is gradually reduced from 1 Hz to 0 Hz). At this time, force shows a linear relationship with voltage (i.e., $f_a = kdu$) [37]. If the unknown term is ignored, then only the linear term remains in the dynamic model [Eq. (5)], and the input and output terms are located on both sides of the equation, which yields the following:

$$m\ddot{x} + b\dot{x} + kx = kdu. \tag{6}$$

The transfer function of the linear system is obtained by the following Laplace transformation of Eq. (6):

$$\frac{X(s)}{U(s)} = \frac{kd}{ms^2 + bs + k}, \tag{7}$$

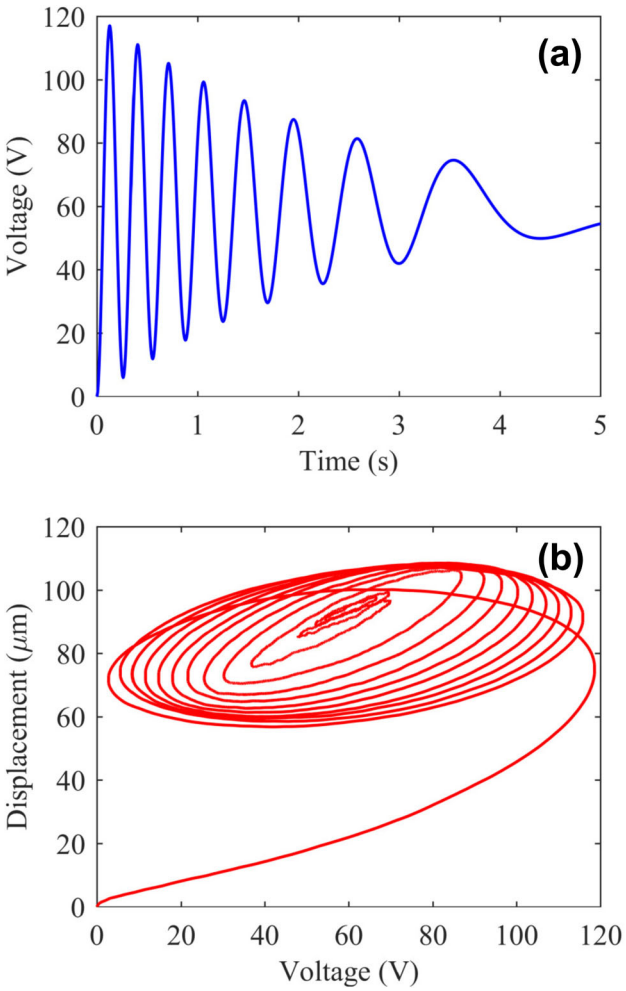

Fig. 3 Open-loop hysteresis test of CPM: **a** sine wave excitation voltage with a gradual attenuation of amplitude and frequency, and **b** voltage–displacement curve of CPM

We can derive $b = 15{,}500$ Ns/m, $k = 9800$ N/m, and $d = 9.78 \times 10^{-7}$ m/V by drawing the frequency response diagram and using MATLAB 2016b system identification toolbox to complete the parameter identification.

Robust controller design

Prior knowledge

Some important knowledge of FO algorithms and TSM is introduced before presenting the controller design.

Definition 1 For a function $f(t)$ with respect to time t, λth-order Riemann–Liouville fractional differential and integral

equations are defined as follows [38]:

$$D^{\lambda} f(t) = \frac{d^{\lambda} f(t)}{dt^{c}\lambda} = \frac{1}{\Gamma(m-\lambda)} \frac{d^{m}}{dt^{m}} \int_{t_0}^{t} \frac{f(\tau)}{(t-\tau)^{\lambda-m+1}} d\tau \tag{8}$$

$${}_{t_0} I_t^{\lambda} f(t) = \frac{1}{\Gamma(\lambda)} \int_{t_0}^{t} \frac{f(\tau)}{(t-\tau)^{1-\lambda}} d\tau \tag{9}$$

$$\Gamma(x) = \int_0^{+\infty} t^{x-1} e^{-t} dt \tag{10}$$

where $m-1 < \lambda \leq m$, $m \in N$, and $\Gamma(\cdot)$ is the Gamma function.

Lemma 1 *For a Lyapunov function $V(x)$, with the any given initial value condition $V(x_0)$, the following first-order differential inequality must be satisfied* [33]

$$\dot{V}(x) + \alpha V(x) + \beta V^{\gamma}(x) \leq 0 \quad 0 < \gamma < 1 \quad \alpha, \beta > 0 \tag{11}$$

$V(x)$ can converge to 0 in finite time, and the stable time can be satisfied by the following inequality

$$T \leq \frac{1}{\alpha(1-\gamma)} \ln \frac{\alpha V^{1-\gamma}(x_0) + \beta}{\beta} \tag{12}$$

Robust controller design

The proposed controller aims to accurately track the desired displacement of CPM despite the presence of uncertain factors, such as external disturbance, hysteretic nonlinearity, or unmodeled items. The displacement, velocity, and acceleration errors are defined as follows:

$$e = x - x_d, \tag{13}$$

$$\dot{e} = \dot{x} - \dot{x}_d, \tag{14}$$

$$\ddot{e} = \ddot{x} - \ddot{x}_d, \tag{15}$$

where x_d, $\dot{x}_d$, and $\ddot{x}_d$ are the desired displacement, velocity, and acceleration, respectively.

The FONTSM manifold ensures the accurate tracking and rapid response of CPM to the expected displacement and can be expressed as follows:

$$s = \dot{e} + pD^{\lambda-1}(\mathrm{sig}(e)^{\alpha}), \tag{16}$$

where $0 < \alpha, \lambda < 1$, and the calculation is simplified into $\mathrm{sig}(e)^{\alpha} = |e|^{\alpha}\mathrm{sign}(e)$.

The following fast-TSM-type reaching law is adopted:

$$\dot{s} = -k_1 s - k_2 \mathrm{sig}(s)^{\beta}, \tag{17}$$

where $0 < \beta < 1$; and gains k_1 and k_2 are positive numbers. The controller then achieves finite-time convergence.

Based on the selected FONTSM manifold s and fast-TSM-type reaching law, the designed FONTSM controller can be expressed as

$$u = \underbrace{\frac{1}{kd}\{m[\ddot{x}_d - pD^{\lambda}(\mathrm{sig}(e)^{\alpha})] + b\dot{x} + kx - m[k_1 s + k_2 \mathrm{sig}(s)^{\beta}]\}}_{\text{FONTSM}} - \underbrace{\frac{m}{kd}\Delta\hat{P}}_{\text{TDE}}, \tag{18}$$

where $\Delta\hat{P}$ is the estimation of ΔP. In traditional methods, the online estimation of $\Delta\hat{P}$ is extremely tedious. Intelligent control methods, such as adaptive control or neural network approximation, are generally used. However, the calculation is highly complex, which is not conducive to engineering applications. Nevertheless, TDE presents a convenient method for calculating $\Delta\hat{P}$. $\Delta\hat{P}$, which is formulated as

$$\Delta\hat{P} = \Delta P(t-L) = \ddot{x}_{(t-L)} - \frac{kd}{m} u_{(t-L)} + \frac{b}{m}\dot{x}_{(t-L)} + \frac{k}{m} x_{(t-L)}, \tag{19}$$

where t represents the current time, and L represents the time-delay parameter. $\Delta P(t-L)$ represents value of ΔP at time $t-L$.

Reducing the time-delay parameter will improve the estimation accuracy of TDE, such that $\Delta P(t) \approx \Delta P(t-L)$. The time-delay parameter can be adopted as an several times of the step size. The TDE error is defined as $\Delta\tilde{P} = \Delta P - \Delta\hat{P}$.

Remark 2 According to Eq. (19), the calculation of $\Delta\hat{P}$ is highly suitable for computer implementation.

Remark 3 Equation (19) reveals that TDE is suitable for the control system without a sudden signal (e.g., impact force, friction, or clearance). The cells are soft, and elastic deformation occurs during puncture, thereby avoiding the impact force. In the mechanical structural design of CPM, a flexible hinge is used as a displacement amplification mechanism to completely prevent friction and clearance and effectively suppresses the TDE error. Therefore, TDE offers great advantages.

According to the simplified dynamic model [Eq. (5)] and combining Eqs. (18) and (19), the control law of the synthetic FONTSM control and TDE technology is formulated as

$$u=\underbrace{\frac{1}{kd}\{m[\ddot{x}_d-pD^{\lambda}(\mathrm{sig}(e)^{\alpha})]+b\dot{x}+kx-m[k_1 s+k_2\mathrm{sig}(s)^{\beta}]\}}_{\text{FONTSM}}-\underbrace{\frac{m}{kd}\{\ddot{x}_{(t-L)}-\frac{kd}{m}u_{(t-L)}+\frac{b}{m}\dot{x}_{(t-L)}+\frac{k}{m}x_{(t-L)}\}}_{\text{TDE}}. \quad (20)$$

By mainly including the FONTSM and TDE terms, the controller can be called FONTSM-TDE.

Remark 4 The proposed controller adopts the continuous and differentiable FONTSM manifold and the fast-TSM-type reaching law to achieve continuous output, prevent chattering, and achieve finite-time convergence. The unknown item is accurately estimated by using TDE and compensated effectively. This technology can effectively reduce the gain parameters of FONTSM and ensure the stability and smoothness of the control law output. The TDE error is compensated by the FONTSM term. Therefore, the FONTSM and TDE items perfectly complement each other.

By substituting the control law [Eq. (20)] into dynamic Eq. (5), a necessary algebra operation leads to the following closed-loop system error equation:

$$\ddot{e}+pD^{\lambda}(\mathrm{sig}(e)^{\alpha})+k_1 s+k_2\mathrm{sig}(s)^{\beta}=\Delta\tilde{P}. \quad (21)$$

Remark 5 The solution of displacement error e is not related to the desired displacement or external disturbance, thereby validating the strong robustness of the controller.

Refer to "Appendix A" and "B" for stability analysis and parameter tuning of the closed-loop system of the controller.

Robust exact differentiator

A laser displacement sensor is proposed in this paper to collect the actual displacement signal. The closed-loop feedback of actual speed and actual acceleration is also required in the designed robust controller (20). Theoretically, the real displacement signal can be differentiated once or twice to obtain the actual velocity or acceleration, respectively. However, in practical applications, a differential operation of the displacement signal can amplify errors or result in differential explosion due to the noise signal that accompanies the displacement signal. The amplification of the noise signal in differential calculation can be restrained, and using the robust precise differentiator (RED) [39] to estimate the full state of the system can obtain results with satisfactory accuracy. In this paper, the full-state estimation is achieved by using RED.

The second-order differentiator of RDE is expressed as

$$\begin{cases}\dot{z}_0=v_0=-\lambda_1|z_0-x|^{2/3}\mathrm{sign}(z_0-x)+z_1\\ \dot{z}_1=v_1=-\lambda_2|z_1-v_0|^{1/2}\mathrm{sign}(z_1-v_0)+z_2\\ \dot{z}_2=-\lambda_3\mathrm{sign}(z_2-v_1)\end{cases} \quad (22)$$

where $\lambda_1=3\lambda^{1/3}$, $\lambda_2=1.5\lambda^{1/2}$, $\lambda_3=1.2\lambda$, $\lambda\geq|x|$. $z_0=\hat{x}$, $z_1=\hat{\dot{x}}$, and $z_2=\hat{\ddot{x}}$ are the estimated values of RED for the displacement, velocity, and acceleration signals, respectively.

Given its direct relationship with the control accuracy of the proposed controller, the performance of RED is tested by conducting a computer simulation experiment. With the desired displacement signal, the performance of RED can be formulated as

$$x=e^{-0.5t}\sin(2\pi t)\ \mu\mathrm{m},$$

Meanwhile, the desired values of speed signal v and acceleration signal a are expressed as

$$v=\dot{x}=-0.5e^{-0.5t}\sin(2\pi t)+2\pi e^{-0.5t}\cos(2\pi t)\ \mu\mathrm{m},$$
$$a=\ddot{x}=[0.25e^{-0.5t}\sin(2\pi t)-\pi e^{-0.5t}\cos(2\pi t)-\pi e^{-0.5t}\cos(2\pi t)-4\pi^2 e^{-0.5t}\sin(2\pi t)]\ \mu\mathrm{m}.$$

To accurately simulate the real signal, the Gaussian white noise signal is added as the input signal to the expected displacement. A larger λ corresponds to a higher RED estimation accuracy and a more serious chattering, whereas a smaller λ corresponds to a lower estimation accuracy and slower convergence speed. $\lambda=0.005$ is determined after trade-off and comparison. Figure 4 shows the RED test results. Despite rapidly estimating the displacement signal with the highest accuracy, RED has a poor acceleration signal estimation accuracy that directly increases the TDE error. However, FONTSM compensates for the defects in TDE precision and guarantees control precision. This viewpoint is verified by the results of the computer simulation and HILS experiments presented in Sects. 4 and 5, respectively.

Based on the designed control law [Eq. (20)], RED is used to realize a real-time estimation of the full state. Figure 5 presents the control system block diagram.

Comparative simulation studies

The proposed controller has a generalized structure and an advanced concept, whereas the conventional controller can be derived from the proposed controller. In this section, computer comparative simulation experiments are performed for various controllers to investigate the performance of the proposed controller.

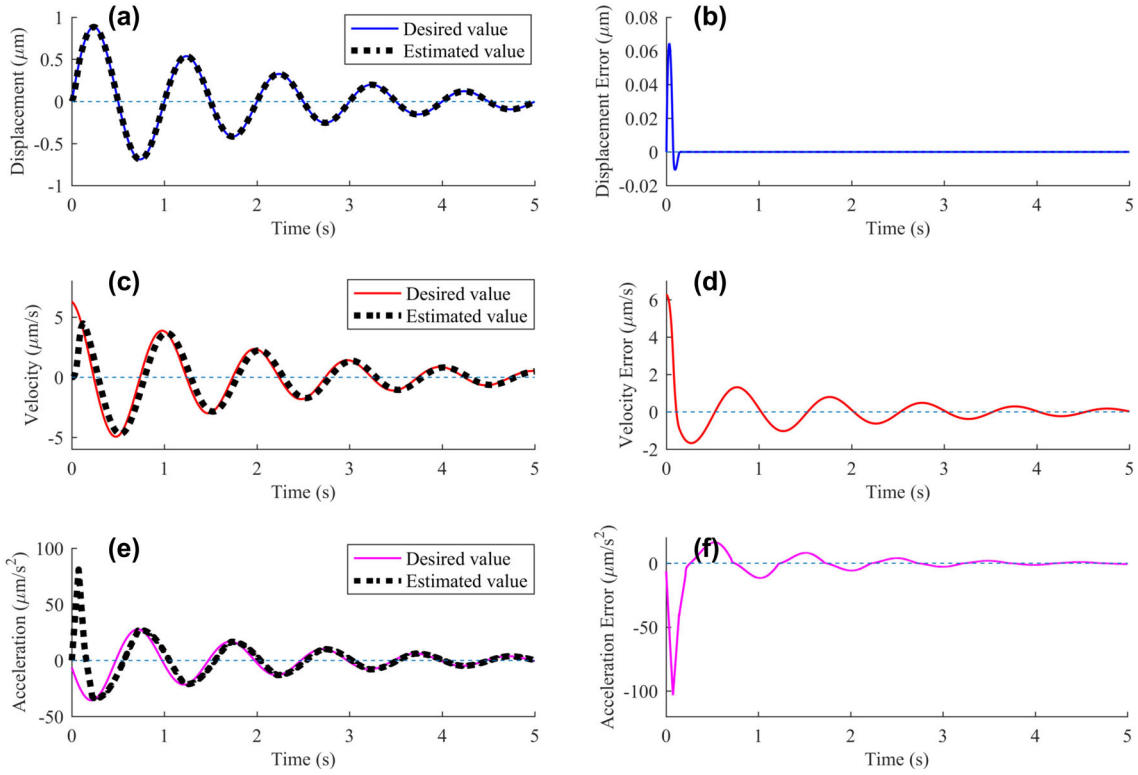

Fig. 4 Performance test of RED by computer simulation. Desired and estimated values of **a** displacement, **c** velocity, and **e** acceleration. **b**, **d**, and **f** are the estimated error of displacement, velocity, and acceleration, respectively

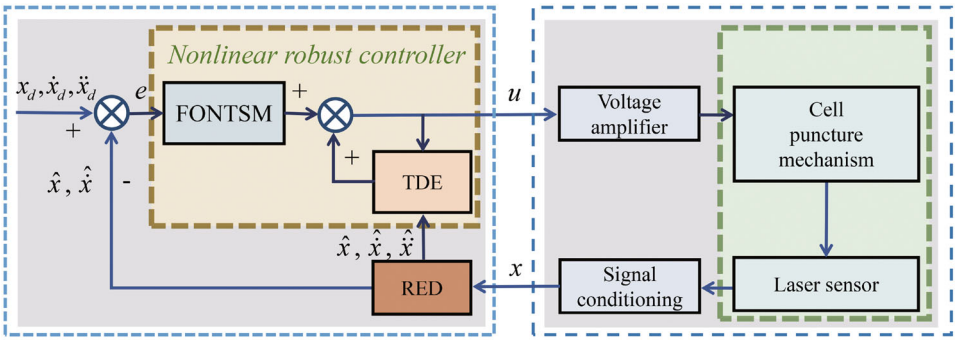

Fig. 5 Controller block diagram of synthesized FONTSM, TDE, and RED technology

Displacement tracking simulation experiment

The performance of the proposed controller in an ideal environment is examined by conducting computer simulation experiments to verify the applicability of this controller to CPM. These experiments are conducted on a computer with a Windows 7 operating system, 3.60 GHz CPU, and 8 G memory. MATLAB/Simulink is adopted as the simulation platform with a step size of 0.1 ms. The system tracks the desired displacement curve of the sine wave, which is expressed as $y = (50 + 50 \times \sin(\pi t - \pi/2))$ μm.

Traditional root-mean-square error (RMSE) and maximum error (ME) are used as evaluation indicators to quantitatively measure the performance of the four controllers.

Trial-and-error method is used to adjust all adjustable parameters one by one from smallest to largest. The satisfying parameters are $\alpha = 0.7, \beta = 0.9, \lambda = 0.9, k = 4 \times 10^{-6}, k_1 = -2 \times 10^4$, and $k_2 = -0.05$. The parameters of the other three controllers are consistent with the above parameters. In MF-FNTSM and Wang's controller, the value of $\bar{m}$ is reduced to play a role similar to low-pass filtering to decrease the influence of noise in the control law and improve control quality.

Table 1 and Fig. 6 show that all four controllers can accurately achieve sinusoidal motion. Although slightly greater than that of MB-FNTSM, the RMSE of the proposed controller is substantially lower than that of the MB-FNTSM controller in terms of ME (Table I). Generally, the proposed

Table 1 Performance index of four controllers in tracking sine wave displacement curve

Performance indicator	Controller			
	MF-FNTSM	MB-FNTSM	Wang's controller	Proposed
RMSE (μ m)	4.91×10^{-4}	1.02×10^{-4}	1.58×10^{-4}	1.11×10^{-4}
ME (μ m)	8.66×10^{-4}	5.22×10^{-4}	4.53×10^{-4}	2.36×10^{-4}

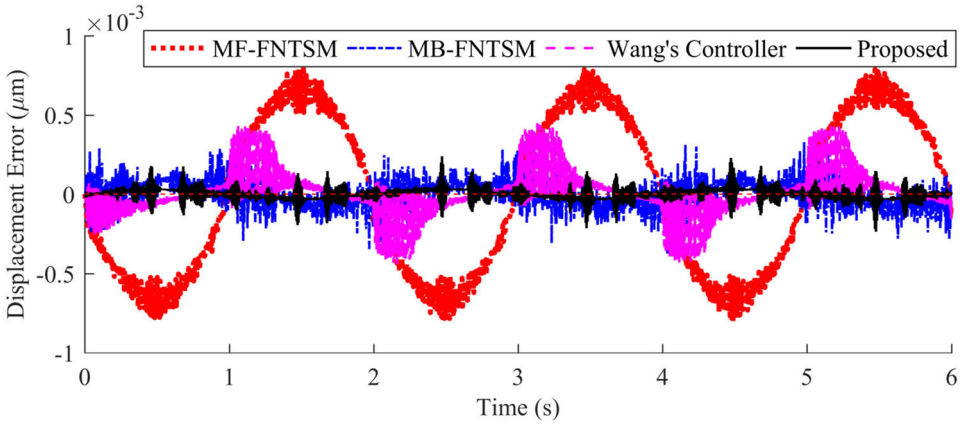

Fig. 6 Displacement error curve of four controllers in tracking the sine wave displacement curve

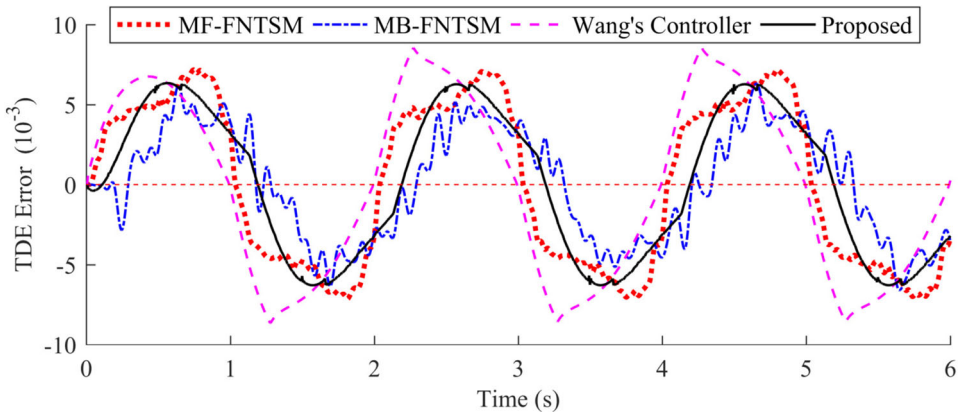

Fig. 7 Estimation error curve of the unknown term in tracking the sine wave displacement: **a** MF-FNTSM, **b** MB-FNTSM, **c** Wang's controller, and **d** proposed controller

controller obtains the highest control accuracy. The displacement error curves of MF-FNTSM and Wang's controller regularly fluctuate, and their fluctuation period is the same as that of the desired displacement. A comparative study of the TDE error of the output terms of the control law is conducted to explain this phenomenon and to reveal the working mechanism of the proposed controller.

The TDE error curve in Fig. 7 is drawn by the TDE error equation $\Delta\tilde{P} = \Delta P - \Delta\hat{P}$. TDE accurately estimates the unknown terms, and the TDE error of the four controllers is controlled in the order of 10^{-3}. Compared with the maximum output value of the control law (60 V), the TDE error is nearly ignored. Moreover, the TDE error curve and desired displacement error curve fluctuate synchronously in MF-FNTSM and Wang's controller. Therefore, the TDE error directly affects control accuracy. However, this phenomenon is not observed in MB-FNTSM and the proposed controller. Therefore, the composition of each item in the control law must be comprehensively investigated.

Figure 8 presents the controller outputs, including total control law (black solid line), sliding mode term (pink dotted line), and TDE term (blue dotted line). For the model-free controllers (i.e., MF-FNTSM and Wang's controller), the output of the sliding mode term is approximately zero, whereas that of the controller depends on the output of the TDE term. The control quality of the TDE term directly determines the greatest overall control effect because the sliding mode and TDE term do not have complementary roles. Meanwhile, the outputs of model-based controllers (i.e., MB-FNTSM and the proposed controller) depend on the combined action of sliding mode and TDE terms. The TDE error fluctuates periodically, but the sliding mode term compensates for the TDE error and achieves precise control. Therefore, MB-FNTSM and the proposed controller obtain the smallest RMSE. u_{TDE} represents the unknown term, whereas u_{FNTSM} or u_{FONTSM}

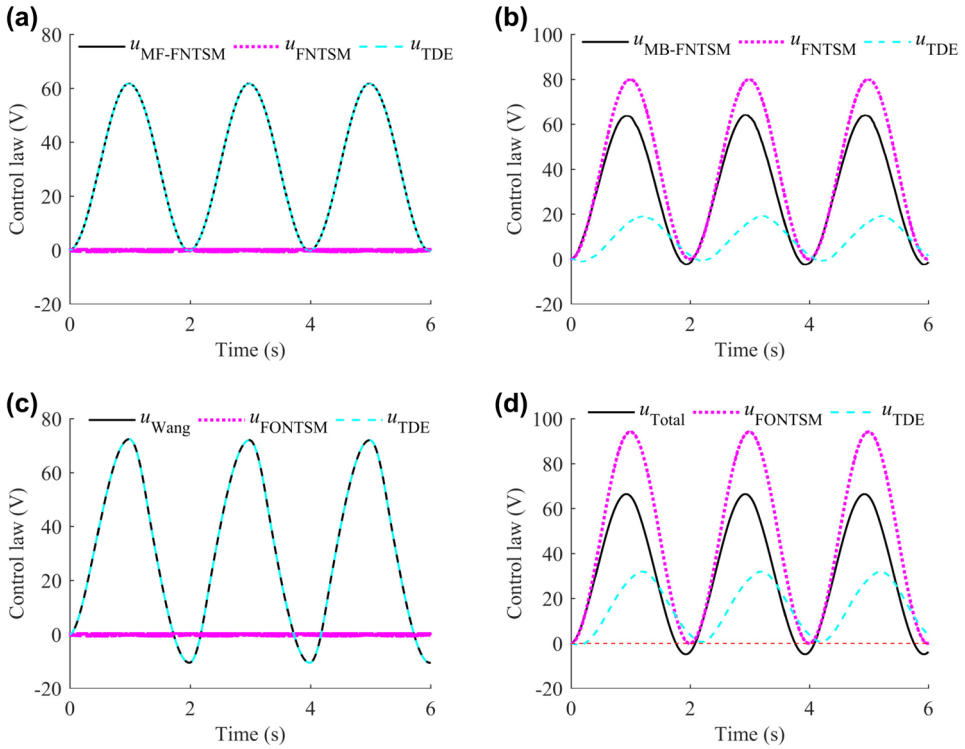

Fig. 8 Output curves of the controller in computer simulation. Total control law (black solid line), sliding mode term (pink dotted line), and TDE term (blue dotted line): **a** MF-FNTSM, **b** MB-FNTSM, **c** Wang's controller, and **d** proposed controller

represent the known term. The proportion of unknown and known items in the model verifies that the dynamic model includes substantial unknown terms, such as hysteretic nonlinearity, disturbance, and unmodeled terms (Fig. 8b, d).

Remark 6 In model-free control, the substantial unknown information must be estimated by using TDE, and control quality can be improved by reducing the value of $\bar{m}$. Therefore, unknown items occupy a dominant position. As a result, the output of the control law heavily depends on the realization of TDE. In engineering applications, the accuracy of TDE is restricted by sensor measurement noise and CPU operation speed, thereby increasing the time-delay parameter and further reducing the control quality. In model-based control, dynamic Eq. (5) contains the physical information of the model, and the proportion of unknown terms is greatly reduced. Therefore, the sliding mode term can play its role and occupy the main position of the control law output. u_{FNTSM} or u_{FONTSM} can achieve finite-time convergence, thereby improving the control accuracy of the controller. Specifically, the FO term in the FONTSM manifold further improves the control effect of SMC.

In model-based control, dynamic Eq. (5) reflects most of the model information, and the proportion of unknown terms is greatly reduced. Therefore, the sliding mode term can play its role and occupy the main position of the control law output. The FONTSM term can achieve finite-time convergence, thereby improving the control accuracy of the controller. Specifically, the FO term in the FONTSM manifold further improves the control effect of SMC.

Semi-physical displacement tracking experiment

The performance of four controllers in a real environment is compared by conducting an HILS experiment [40].

Experimental setup

Figure 9 shows the HILS system constructed by xPC Target. Figure 10 shows the hardware system used in the cell puncture displacement tracking experiment. xPC Target provides a complete solution of rapid prototyping and HILS and can implement the control strategy of the Simulink program running on a PC to act on a physical device. The PEAs and voltage amplifiers are obtained from Harbin Core Tomorrow Science Technology Co., Ltd., and their models are Pst120/7/20VS12 and E00.6, respectively. The laser displacement sensor is obtained from KEYENCE Corporation, and its model and resolution are lk-h020 and 0.02 μm, respectively.

MATLAB/Simulink 2016b is used to build the controller on the host computer, to compile and generate the target code, and to download this code to the target computer. After converting the digital signal output of the target computer into an analog voltage signal, this signal is outputted

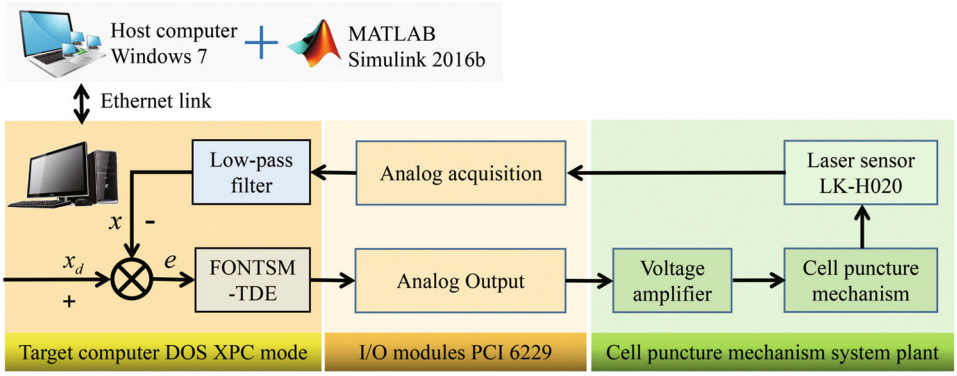

Fig. 9 Construction of HILS system of CPM based on xPC Target technology

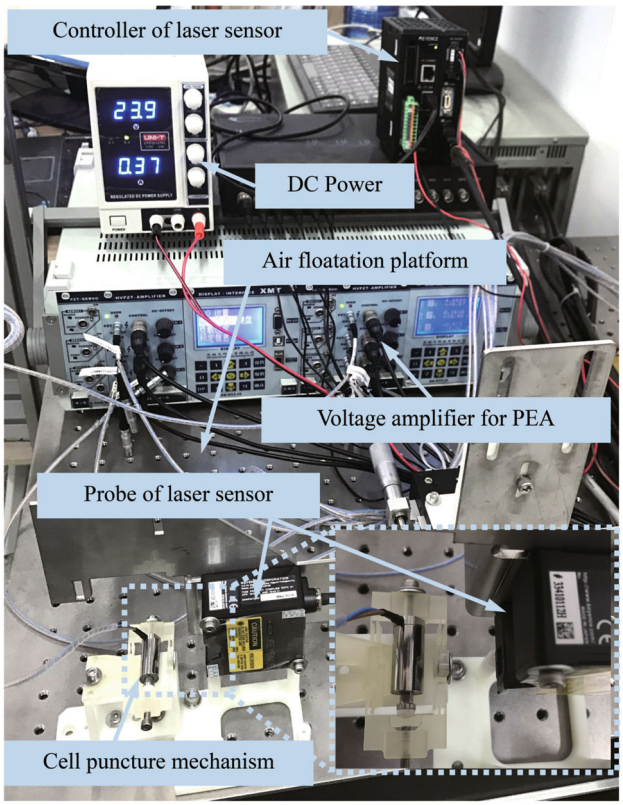

Fig. 10 Global picture and local structure of displacement tracking experiment of CPM

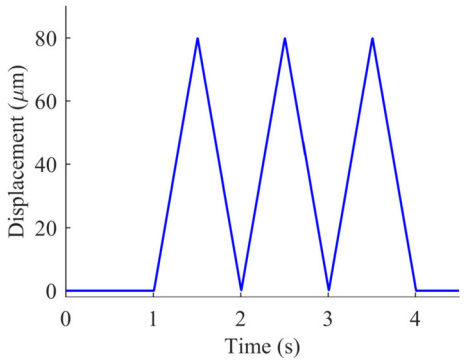

Fig. 11 Triangular curve as the desired displacement in the HILS experiment

to the voltage amplifier and drives the CPM to move. After the analog/digital conversion, the analog displacement signal collected by the laser displacement sensor is fed back to the target computer. The HILS system is then constructed.

HILS experiment

The controller design must consider tracking the continuous and differentiable trajectory curve. However, a continuous yet undifferentiable trajectory curve is tracked in the HILS experiment to comprehensively examine the performance of the controller. This situation presents a challenge to the controller and can test its effectiveness in real engineering applications. Therefore, further research is necessary. Figure 11 shows the desired displacement curve.

The displacement error curve in Fig. 12 and the performance index in Table 2 indicate that compared with the computer simulation results, the accuracy of HILS is reduced under the effects of sensor resolution, measurement noise, and external disturbance. However, the four controllers can achieve an accurate triangular motion. The proposed controller has the highest control accuracy with an RMSE of 0.041 μm and ME of 0.204 μm. Meanwhile, MF-FNTSM obtains the lowest control accuracy, MB-FNTSM and Wang's controller obtain a similar ME, and MB-FNTSM achieves a low error fluctuation. In other words, the performance ranking obtained in the HILS experiment is similar to that obtained in the computer simulation.

Figure 13 shows the output curves of the controller in the HILS experiment, including the total control law (black solid line), sliding mode term (pink dotted line), and TDE term (blue dotted line) with evident chattering phenomenon. The controller shows smooth output curves in the computer simulation experiment, which suggests that measurement noise and disturbance in engineering applications can drive the chattering of the control law.

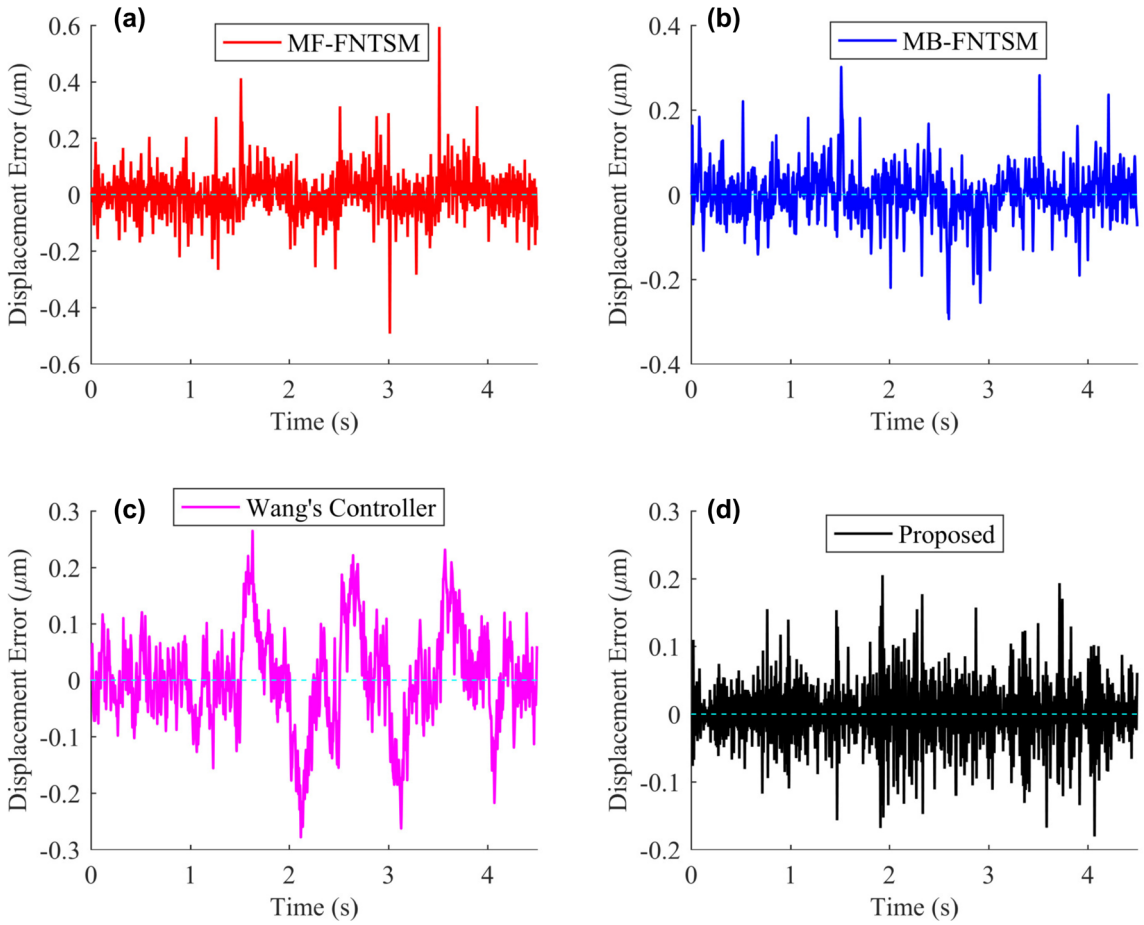

Fig. 12 Displacement error curve of four controllers when tracking the triangular curve: **a** MF-FNTSM, **b** MB-FNTSM, **c** Wang's controller, and **d** proposed controller

Table 2 Performance index of four controllers in tracking the triangular curve

Performance indicator	Controller			
	MF-FNTSM	MB-FNTSM	Wang's controller	Proposed
RMSE (μm)	0.077	0.057	0.093	0.041
ME (μm)	0.532	0.294	0.298	0.204

Figure 13a, c shows that in the model-free controller, the FNTSM or FONTSM term oscillates near the zero line, whereas the output curve of the total control law coincides with the output of the TDE term. Figure 13b, d indicates that in model-based controllers, the proportion of the TDE term is considerably reduced, and the sliding mode and TDE terms have a high proportion of output. These phenomena are consistent with the computer simulation results.

Remark 7 For model-based controllers, the proportion of the TDE term in the control law is reduced because the dynamic model vividly describes the physical model of the system. The sliding mode term successfully compensates for the deficiencies of the TDE error and has a high control quality.

Remark 8 In the HILS experiment, the output of the control law shows apparent chattering, and the accuracy control is considerably reduced due to the unfavorable constraints of sensor resolution, measurement noise, and external disturbance compared with the computer simulation experiment. However, the proposed controller retains the highest control accuracy. The proposed controller also shows high stability, strong robustness, and precise control accuracy and can drive the CPM to achieve a precise trajectory tracking control.

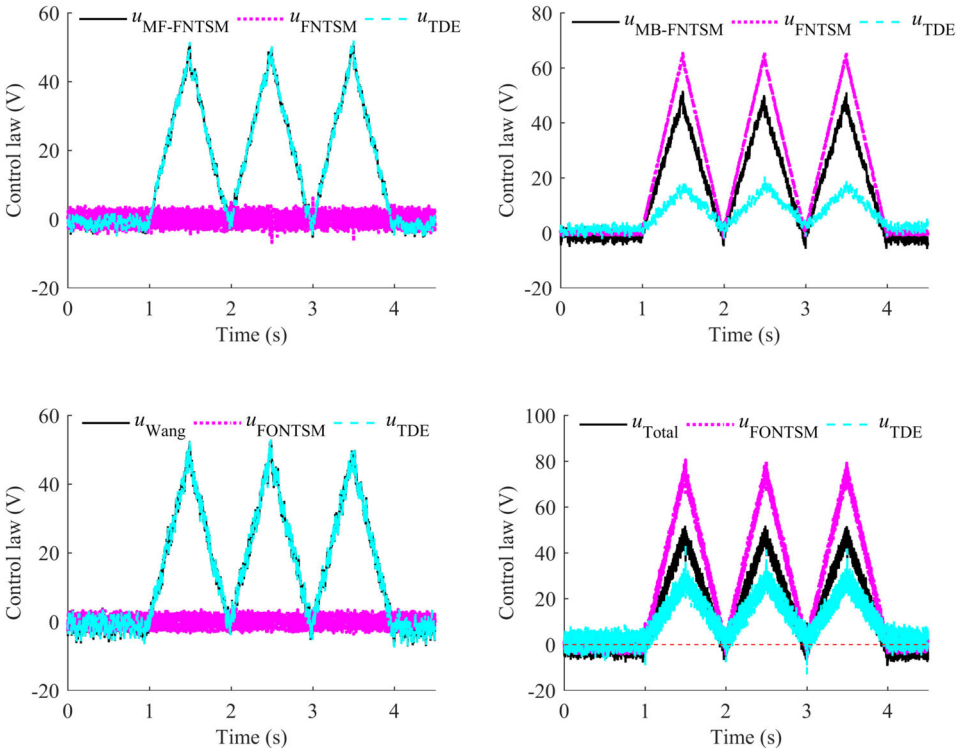

Fig. 13 Output curves of the controller in the HILS experiment, including the total control law (black solid line), sliding mode term (pink dotted line), and TDE term (blue dotted line): **a** MF-FNTSM, **b** MB-FNTSM, **c** Wang's controller, and **d** proposed controller

Cell puncture experiment

Zebrafish and human genes have 87% familiarity [41]. Therefore, zebrafish has become the third most widely used vertebrate model organism used in life science research after mice and rats [42]. Disease research, new drug development, chemical safety, and environmental toxicology monitoring can be realized by injecting different substances into zebrafish embryos. These embryos must complete a large sample volume of microinjection within a few hours after spawning [43]. Therefore, puncturing zebrafish embryo efficiently and accurately offers great biological value. In addition, zebrafish embryos are transparent, thereby facilitating the observation of cell micro-puncture. Accordingly, zebrafish embryo is treated as the research object in this study to test the performance of CPM and robust controller.

Figure 14 presents the experimental environment of the zebrafish embryo micro-puncture. The CPM is installed on the inverted biological microscope (model: BA1000; Chongqing Optical Instrument Factory). The zebrafish embryo is located in the field of view of the electron microscope (resolution: 30 million pixels), and the puncture process is played in real time through the computer screen. To prevent the zebrafish embryo from being scratched, the end of the holding pipette is polished, and the zebrafish embryo is adsorbed on the end of the holding pipette by negative pressure. The end of the injecting pipette has a diameter of 5 μm to prevent the cell puncture from damaging the zebrafish

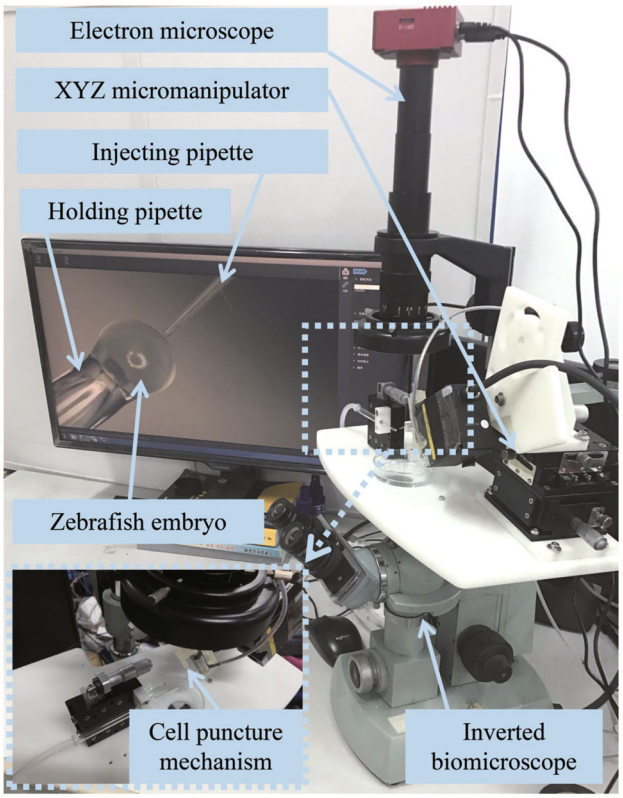

Fig. 14 Zebrafish embryo micro-puncture experiment under an electron microscope

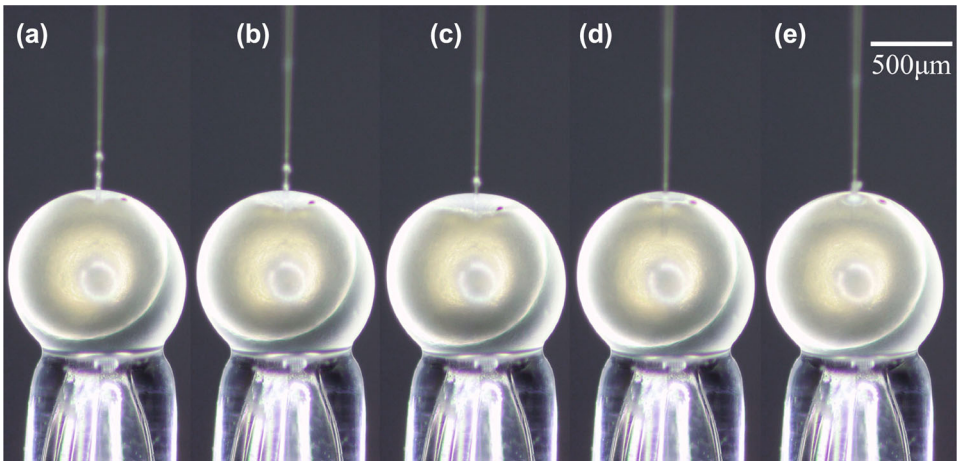

Fig. 15 Electron microscopic pictures of zebrafish embryo for micro-puncture. **a** Injecting the pipette effortlessly contacts the outside of the cell membrane. **b**, **c** CPM continuously increases the displacement and feed, and the injecting pipette causes the cell membrane to deform substantially. **d** Head of the injecting pipette entering the zebrafish embryo and reaching the designated position. **e** Injecting pipette exiting from the zebrafish embryo

embryo. Driven by CPM, the injecting pipette penetrates the cell membrane, reaches the designated cell tissue, and exits the cell membrane. Figure 15 shows the entire puncture process.

Conclusion

This study designs a novel, nonlinear robust controller for a newly developed CPM driven by PEAs. To facilitate engineering applications, the dynamic model of CPM is locally optimized. The new controller is based on the simplified Bouc–Wen dynamic model, which includes TDE and FONTSM terms. The real-time estimation and effective compensation of unknown items are realized via TDE. The FONTSM term adopts the FONTSM manifold and fast-TSM-type reaching law, which can achieve finite-time convergence and high control accuracy. The stability of the developed scheme is proven by Lyapunov theory. For the proposed controller, the output of the FONTSM term accounts for a large proportion, and the FONTSM term can compensate for the TDE error because the physical model is described comprehensively by the dynamic model. Compared with IO or model-free controllers, the proposed controller has stronger robustness and higher control accuracy. The cell puncture experiments reveal that the proposed controller can accurately control the micro-puncture mechanism to effectively micro-puncture zebrafish embryos.

Puncture force is introduced in the robust controller to further improve the cell survival rate. The displacement and expected force are used as tracking targets before and during the cell puncture process, respectively. Future studies should track the force and displacement signals simultaneously in the cell puncture process and realize compliance control.

Acknowledgements This work was supported by the Zhejiang Public Welfare Technology Application Research Support Project (Grant No. LGG20E050012), Foreign Experts Affairs Foundation (Grant No. G20190010180), National Natural Science Foundation of China (Grant No. 51975277). The authors gratefully acknowledge these support agencies.

Author contributions Shengdong Yu participated in the study design, data analysis, experimental research, writing and editing of the manuscript. Hongtao Wu, Mingyang Xie, and Haiping Lin participated in the study design, Jinyu Ma performed the writing and editing of the manuscript and data analysis. All authors have read and approved the final manuscript and, therefore, have full access to all the data in the study and take responsibility for the integrity and security of the data.

Compliance with ethical standards

Conflict of interest The authors declare that there is no conflict of interest.

Ethical approval This article does not contain any studies with human or animal subjects performed by any of the authors.

Appendix

Stability analysis

For TDE error $\Delta\tilde{P}$, a positive number φ makes $\Delta\tilde{P}$ bounded, i.e., $|\Delta\tilde{P}| \leq \varphi$. The boundedness certificate of $\Delta\tilde{P}$ can be referred to [35] and [36].

Definition 2 For the CPM described in Eqs. (1) and (2), if the FONTSM manifold represented by Eq. (16) and the fast-TSM-type reaching law represented by Eq. (17) are adopted, then the closed-loop system can achieve finite-time stability under the action of the proposed controller [Eq. (20)]. The system-state trajectory can converge to the following range:

$$|s| \leq \min\{d_1, d_2\} \quad d_1 = \frac{\varphi}{k_1} \quad d_2 = \left(\frac{\varphi}{k_2}\right)^{1/\beta}. \tag{23}$$

The proof of Definition 2 and the stability of the closed-loop system are demonstrated by using Lyapunov theory.

Proof A Lyapunov function is established as follows:

$$V = \frac{1}{2}s^2. \tag{24}$$

The above function is differentiated with respect to time and then combined with FONTSM manifold (16) to obtain

$$\dot{V} = s(\ddot{e} + pD^{\lambda}\mathrm{sig}(e)^{\alpha}). \tag{25}$$

Equation (21) is substituted in the above equation and yields

$$\dot{V} = -s(k_1 s + k_2\mathrm{sig}(s)^{\beta} - \Delta\tilde{P}). \tag{26}$$

Combined with boundary condition $|\Delta\tilde{P}| \leq \varphi$, the above equation can be written as

Combined with boundary condition $|\Delta\tilde{P}| \leq \varphi$, the above equations are transformed into inequality, as follows:

$$\dot{V} \leq -s(k_1 s + k_2\mathrm{sig}(s)^{\beta} - \varphi).$$

The above inequality can be converted into the bellowing forms:

$$\dot{V} \leq -s\left[\left(k_1 - \frac{\varphi}{s}\right)s + k_2\mathrm{sig}(s)^{\beta}\right], \tag{27}$$

$$\dot{V} \leq -s\left[k_1 s + \left(k_2 - \frac{\varphi}{\mathrm{sig}(s)^{\beta}}\right)\mathrm{sig}(s)^{\beta}\right]. \tag{28}$$

For Eq. (27), if $|s| > \varphi/k_1$, then $\dot{V} < 0$. Thus, Eq. (27) can be rewritten as follows:

$$\dot{V} \leq -s(\bar{k}_1 s + k_2\mathrm{sig}(s)^{\beta}) = -\bar{k}_1 s^2 - sk_2\mathrm{sig}(s)^{\beta}, \tag{29}$$

where $\bar{k}_1 = k_1 - \frac{\varphi}{s}$.

Equation (29) is re-arranged as

$$\dot{V} + 2\bar{k}_1 V + 2^{\frac{1+\beta}{2}}k_2 V^{\frac{1+\beta}{2}} \leq 0. \tag{30}$$

According to Lemma 1, V converges to 0 in a finite time. The convergence time T_1 satisfies

$$T_1 \leq \frac{1}{\bar{k}_1(1-\beta)}\ln\left(\frac{2\bar{k}_1 V_1^{\frac{1-\beta}{2}}(x_0)}{2^{\frac{1+\beta}{2}}k_2} + 1\right). \tag{31}$$

In finite time T_1, the system-state trajectory s converges to the following region:

$$|s| \leq \frac{\varphi}{k_1} = d_1. \tag{32}$$

Using similar analysis for Eq. (28), if $|s|^{\beta} > \varphi/k_2$, then $\dot{V} < 0$. Thus, Eq. (28) can be rewritten as follows:

$$\dot{V} \leq -s(k_1 s + \bar{k}_2\mathrm{sig}(s)^{\beta}) = -k_1 s^2 - s\bar{k}_2\mathrm{sig}(s)^{\beta}, \tag{33}$$

where $\bar{k}_2 = k_2 - \frac{\varphi}{\mathrm{sig}(s)^{\beta}}$.

Equation (33) is re-arranged as follows:

$$\dot{V} + 2k_1 V + 2^{\frac{1+\beta}{2}}\bar{k}_2 V^{\frac{1+\beta}{2}} \leq 0, \tag{34}$$

According to Lemma 1, V converges to 0 in a finite time. The convergence time T_2 satisfies

$$T_2 \leq \frac{1}{k_1(1-\beta)}\ln\left(\frac{2k_1 V_1^{\frac{1-\beta}{2}}(x_0)}{2^{\frac{1+\beta}{2}}\bar{k}_2} + 1\right), \tag{35}$$

In finite time T_2, the system-state trajectory s converges to the following region:

$$|s| \leq \left(\frac{\varphi}{\bar{k}_2}\right)^{\frac{1}{\beta}} = d_2, \tag{36}$$

In sum, the system-state trajectory converges to the following range in finite time:

$$|s| \leq \min\{d_1, d_2\}.$$

Therefore, the stability of the closed-loop system is certain, and the proof of Definition 2 is completed. □

Controller Adjustment

Six parameters, namely, α, β, k, k_1, k_2, and λ, must be tuned in the proposed controller.

Remark 9 From Eqs. (31) and (35), a smaller β corresponds to a shorter convergence time of the system-state trajectory and a higher accuracy of the control system.

Remark 10 From Eqs. (16), (17), and (20), when $\alpha \to 1, \beta \to 1,$, the sign function disappears, and the controller shows linear characteristics. When $\alpha \to 0, \beta \to 0$, the control law is discontinuous under the influence of the symbolic function. Therefore, $0 < \alpha, \beta < 1$ ensures that the controller exhibits not only the chattering-free characteristics of linear control but also the strong, robust characteristics of a discontinuous controller.

Remark 11 From Eq. (23), the k_1 and k_2 gains of the reaching law affect the convergence region of the state trajectory. Gains k_1 and k_2 must be satisfied as $k_1 = k_2 > |\Delta\tilde{P}|$ to make the state trajectory converge to a small region as soon as possible.

Remark 12 The FO term $D^{\lambda}(\mathrm{sig}(e)^{\alpha})$ can enhance the sign function and show a large amplitude when the sign of displacement error changes. When $\lambda \to 1$, the amplitude increases. When $\lambda \to 0$, the effect of FO is weakened and reduced to IO. p is used to increase the variation amplitude of the FO term.

Three Controllers for Comparison

Three existing controllers are derived from the proposed controller as prototypes in the comparative experiments. These three controllers use the FONTSM manifold, the fast-TSM-type reaching law, and the TDE technology to build an FO controller without a model and apply the NTSM manifold, the fast-TSM-type reaching law, and the TDE technology to build an IO controller whether based on a model or not.

Control 1: Wang's controller

The model of system dynamics (1) and (2) is simplified as

$$\bar{m}\ddot{x} + N(x, \dot{x}, \ddot{x}, k, d, h, \tau_d) = u, \tag{37}$$

where $N(x, \dot{x}, \ddot{x}, k, d, h, \tau_d) = \left(\frac{m}{kd} - \bar{m}\right)\ddot{x} + \frac{1}{k}\dot{x} + \frac{1}{d}x + \frac{h}{d} - \frac{\tau_d}{kd}$. To simplify the expression, $N(t)$ represents state of $N(x, \dot{x}, \ddot{x}, k, d, h, \tau_d)$ at time t, and the simplified dynamic model is reformulated as

$$\bar{m}\ddot{x} + N(t) = u. \tag{38}$$

Based on dynamic model (38), $N(t)$ is estimated by TDE technology and is expressed as

$$N(t) \approx \hat{N}(t) = N(t - L) = u(t - L) - \bar{m}\ddot{x}(t - L). \tag{39}$$

The FONTSM sliding surface and fast-TSM-type reaching law described in Eqs. (16) and (17) are used to construct a model-free, robust controller based on FONTSM and TDE. The designed control law imitates the following design ideas and methods of the control law provided in [44]:

$$u = \bar{m}(\ddot{x}_u + pD^{\lambda}(\mathrm{sig}(e)^{\alpha}) + k_1 s + k_2 \mathrm{sig}(s)^{\beta}) + u_{(t-L)} - \bar{m}\ddot{x}_{(t-L)}. \tag{40}$$

According to its proponent [44], this controller is called the Wang's controller.

Control 2: MB-FNTSM controller

If $\lambda = 0$, then the FO function in the controller is lost. The NTSM manifold is formulated as

$$s = \dot{e} + p\mathrm{sig}(e)^{\alpha}, \tag{41}$$

By using the fast-TSM-type reaching law [Eq. (17)] and the dynamic model [Eq. (5)], the controller is constructed as

$$u = \underbrace{\frac{1}{kd}\{m[\ddot{x}_d - p\alpha\dot{e}|e|^{\alpha-1}] + b\dot{x} + kx - m(k_1 s + k_2 \mathrm{sig}(s)^{\beta})\}}_{\text{FNTSM}} - \underbrace{\frac{m}{kd}\Delta\hat{P}}_{\text{TDE}}. \tag{42}$$

NTSM manifold and fast-TSM-type reaching law are adopted in the sliding mode term of the proposed controller. This term is labeled FNTSM, and the model-based controller is abbreviated to MB-FNTSM for convenience.

Substituting the control law [Eq. (42)] into the dynamic model [Eq. (5)] leads to the following displacement error equation of the closed-loop system:

$$\ddot{e} + p\alpha\dot{e}\mathrm{sig}(e)^{\alpha-1} + k_1 s + k_2 \mathrm{sig}(s)^{\beta} = \Delta\tilde{P}, \tag{43}$$

The difference between Eqs. (21) and (43) is called the FO term. A stability analysis of the MB-FNTSM controller can also be completed by referring to the analysis of the proposed controller.

Control 3: MF-FNTSM controller

Let $\lambda = 0$. Then, the MB-FNTSM controller can be designed.

The unknown term is estimated by Eq. (39) using the dynamic model [Eq. (38)], NTSM manifold [Eq. (41)], and fast-TSM-type reaching law [Eq. (17)]. The control law can be designed by referring to the idea presented in [28] as shown below:

$$u = \underbrace{\bar{m}(\ddot{x}_a + p\alpha\dot{e}|e|^{\alpha-1} + k_1 s + k_2 \mathrm{sig}(s)^{\beta})}_{\text{FNTSM}} + \underbrace{u_{(t-L)} - \bar{m}\ddot{x}_{(t-L)}}_{\text{TDE}}. \tag{44}$$

The controller is abbreviated as MF-FNTSM.

Remark 13 The complexity of the controller reflects the required amount of calculation and debugging. The four controllers are ranked as follows in a descending order according to their required amount of calculation: proposed controller>Wang's controller>MB-FNTSM>MF-FNTSM. In engineering applications, the control accuracy and calculation amount of these controllers can be comprehensively balanced to determine the appropriate controller.

References

1. Krishnamoorthy C X Srikumar, Zhang Zhengyi (2020) Guided cell migration on a graded micropillar substrate. Bio-des Manuf 3(1):60–70
2. Permana S, Grant E, Walker GM, Yoder JA (2016) A review of automated microinjection systems for single cells in the embryogenesis stage. IEEE-ASME Trans Mechatron 21(5):2391–2404
3. Lu Z, Chen PCY, Nam J, Ge R, Lin W (2007) A micromanipulation system with dynamic force-feedback for automatic batch microinjection. J Micromech Microeng 17(2):314–321
4. Liu X, Kim K, Zhang Y, Sun Y (2009) Nanonewton force sensing and control in microrobotic cell manipulation. Int J Robot Res 28(8):1065–1076
5. Ock WL Jingyu (2020) A high-throughput three-dimensional cell culture platform for drug screening. Bio-des Manuf 3(1):40–47
6. Wang W, Liu X, Gelinas D, Ciruna B, Sun Y (2007) A fully automated robotic system for microinjection of zebrafish embryos. PLoS One 2(9):1
7. Xie M, Shakoor A, Shen Y, Mills JK, Sun D (2019) Out-of-plane rotation control of biological cells with a robot-tweezers manipulation system for orientation-based cell surgery. IEEE Trans Biomed Eng 66(1):199–207
8. Sun Y, Nelson BJ (2002) Biological cell injection using an autonomous microrobotic system. Int J Robot Res 21(10):861–868
9. Kuchimaru T, Kataoka N, Nakagawa K, Isozaki T, Miyabara H, Minegishi M, Kadonosono T, Kizakakondoh S (2018) A reliable murine model of bone metastasis by injecting cancer cells through caudal arteries. Nat Commun 9(1):2981
10. Liu X, Fernandes R, Gertsenstein M, Perumalsamy A, Lai I, Chi MMY, Moley KH, Greenblatt E, Jurisica I, Casper RF et al (2011) Automated microinjection of recombinant BCL-x into mouse zygotes enhances embryo development. PLoS One 6(7):1
11. Ma L, Xu X, Jiang W (2019) One-dimensional microstructure-assisted intradermal and intracellular delivery. Bio-des Manuf 2(2):24–30
12. Ingber DE (2003) Tensegrity I. Cell structure and hierarchical systems biology. J Cell Sci 116(7):1157–1173
13. Yu S, Xie M, Wu H, Ma J, Li Y, Gu H (2020) Composite proportional-integral sliding mode control with feedforward control for cell puncture mechanism with piezoelectric actuation. ISA Trans. https://doi.org/10.1016/j.isatra.2020.02.015
14. Wang C, Lou X, Xia T, Tian S (2017) The dielectric, strain and energy storage density of BNT-BKHXT1-x piezoelectric ceramics. Ceram Int 43(12):9253–9258
15. Zhang Y, Wang S, Chen C, Zhang N, Wang A, Zhu Y, Cai F (2018) Reduced hysteresis of KNNS-BNKZ piezoelectric ceramics through the control of sintering temperature. Ceram Int 44(11):12435–12441
16. Xu Q (2017) Precision motion control of piezoelectric nanopositioning stage with chattering-free adaptive sliding mode control. IEEE Trans Autom Sci Eng 14(1):238–248
17. Moheimani SOR, Vautier BJG (2005) Resonant control of structural vibration using charge-driven piezoelectric actuators. IEEE Trans Control Syst Technol 13(6):1021–1035
18. Main JA, Garcia E, Newton DV (1995) Precision position control of piezoelectric actuators using charge feedback. J Guid Control Dyn 18(5):1068–1073
19. Xiao S, Li Y (2013) Modeling and high dynamic compensating the rate-dependent hysteresis of piezoelectric actuators via a novel modified inverse preisach model. IEEE Trans Control Syst Technol 21(5):1549–1557
20. Zhang A, Wang B (2014) The influence of maxwell stresses on the fracture mechanics of piezoelectric materials. Mech Mater 68:64–69
21. Lin C, Lin P (2012) Tracking control of a biaxial piezo-actuated positioning stage using generalized duhem model. Comput Math Appl 64(5):766–787
22. Jiang H, Ji H, Qiu J, Chen Y (2010) A modified prandtl-ishlinskii model for modeling asymmetric hysteresis of piezoelectric actuators. IEEE Trans Ultrason Ferroelectr Freq Control 57(5):1200–1210
23. Rakotondrabe M (2011) Bouc-wen modeling and inverse multiplicative structure to compensate hysteresis nonlinearity in piezoelectric actuators. IEEE Trans Autom Sci Eng 8(2):428–431
24. Wen Z, Ding Y, Liu P, Ding H (2019) An efficient identification method for dynamic systems with coupled hysteresis and linear dynamics: Application to piezoelectric-actuated nanopositioning stages. IEEE-ASME Trans Mechatron 24(1):326–337
25. Wu L, Gao Y, Liu J, Li H (2017) Event-triggered sliding mode control of stochastic systems via output feedback. Automatica 82(82):79–92
26. Li H, Shi P, Yao D, Wu L (2016) Observer-based adaptive sliding mode control for nonlinear markovian jump systems. Automatica 64(64):133–142
27. Yu S, Xie M, Wu H, Ma J, Wang R, Kang S (2019) Design and control of a piezoactuated microfeed mechanism for cell injection. Int J Adv Manuf Technol 105(12):4941–4952
28. Yu S, Ma J, Wu H, Kang S (2019) Robust precision motion control of piezoelectric actuators using fast nonsingular terminal sliding mode with time delay estimation. Measurem Control 52:11–19
29. Fallaha C, Saad M, Kanaan HY, Alhaddad K (2011) Sliding-mode robot control with exponential reaching law. IEEE Trans Industr Electron 58(2):600–610
30. Xie M, Li X, Wang Y, Liu Y, Sun D (2018) Saturated pid control for the optical manipulation of biological cells. IEEE Trans Control Syst Technol 26(5):1909–1916
31. Xie M, Shakoor A, Li C, Sun D (2019) Robust orientation control of multi-dof cell based on uncertainty and disturbance estimation. Int J Robust Nonlinear Control 29(14):4859–4871
32. Feng Y, Yu X, Man Z (2002) Brief non-singular terminal sliding mode control of rigid manipulators. Automatica 38(12):2159–2167
33. Yu S, Yu X, Stonier RJ (2003) Continuous finite-time control for robotic manipulators with terminal sliding modes. Automatica 41(11):1957–1964
34. Kang S, Wu H, Yang X, Li Y, Wang Y (2020) Fractional-order robust model reference adaptive control of piezo-actuated active vibration isolation systems using output feedback and multi-objective optimization algorithm. J Vib Control 26(1–2):19–35
35. Lee J, Chang PH, Jin M (2017) Adaptive integral sliding mode control with time-delay estimation for robot manipulators. IEEE Trans Industr Electron 64(8):6796–6804
36. Jin M, Lee J, Ahn KK (2015) Continuous nonsingular terminal sliding-mode control of shape memory alloy actuators using time delay estimation. IEEE-ASME Trans Mechatron 20(2):899–909
37. Ismail M, Ikhouane F, Rodellar J (2009) The hysteresis Bouc–Wen model, a survey. Arch Comput Methods Eng 16(2):161–188
38. Kilbas A, Srivastava H, Trujillo J (2006) Fractional integrals and fractional derivatives. In: Theory and applications of fractional differential equations, pp 69–133
39. Levant A (2003) Higher-order sliding modes, differentiation and output-feedback control. Int J Control 76:924–941
40. Jia F, Cai X, Lou Y, Li Z (2017) Interfacing technique and hardware-in-loop simulation of real-time co-simulation platform for wind energy conversion system. Iet Gen Transm Distrib 11(12):3030–3038
41. Lepanto P, Zolessi FR, Badano JL (2019) Studying human genetic variation in zebrafish. In: Cellular and animal models in human genomics research. Elsevier, pp 89–117
42. Nasevicius A, Ekker SC (2000) Effective targeted gene 'knockdown' in zebrafish. Nat Genet 26(2):216–220

43. Lee WS, Cho H-J, Kim E, Huh YH, Kim H-J, Kim B, Kang T, Lee J-S, Jeong J (2019) Bioaccumulation of polystyrene nanoplastics and their effect on the toxicity of au ions in zebrafish embryos. Nanoscale 11(7):3173–3185

44. Wang Y, Gu L, Xu Y, Cao X (2016) Practical tracking control of robot manipulators with continuous fractional-order nonsingular terminal sliding mode. IEEE Trans Industr Electron 63(10):6194–6204